High Performance CO Gas Sensor Based on ZnO Nanoparticles

M. Hjiri[1,2] · F. Bahanan[1] · M. S. Aida[1,3] · L. El Mir[2] · G. Neri[4]

Abstract

Carbon monoxide sensor was fabricated using ZnO nanoparticles, synthesized by sol–gel technique, as sensing layer. The morphology and structure of the prepared nanopowder were analyzed using X-ray diffraction (XRD), scanning and transmission electron microscopies (SEM and TEM). Photoluminescence (PL) measurements were carried to investigate the defects in ZnO. The sensing tests were performed by a homemade setup. XRD pattern indicate that the prepared ZnO nanopowder has a crystallite size average around 50 nm. TEM and SEM images reveal that the ZnO nanopowder is formed of agglomeration of spherical particles with a size of 50 nm which is in good agreement with XRD analysis. The prepared gas sensor exhibits a response of 74% towards 80 ppm of CO gas with a response/recovery times of 21 and 70 s, respectively at 250 °C and high stability with time. The good sensing properties of ZnO nanoparticles towards CO gas indicate their potential application for the fabrication of low power and highly selective sensors.

Keywords Zinc oxide · Nanoparticles · Selectivity · Sensor · CO

1 Introduction

In the last years, gas sensors based on various semiconducting metal oxides, such as tin oxide [1], iron oxide [2], copper oxide [3], titanium oxide [4], gallium oxide [5] and zinc oxide [6], have attracted the attention of several researchers. These metal oxide sensors exhibited strong response and fast response/recovery times, in addition of good selectivity, stability, compatibility with microelectronic devices [7].

Among them, ZnO has been shown to be useful materials for monitoring various pollutant gases like CO, benzene, ammonia, CO_2, NOx. Zinc oxide is an n-type semiconductor with a direct wide band gap (3.3 eV) [8–10]. This material found broad ranging applications in varistors [11], surface acoustic wave (SAW) devices [12], transparent conducting oxide electrodes [13], solar cells [14], blue/UV light emitting devices [15], gas sensors [16, 17], etc.… Its conductivity can be tailored by controlling the deviation from stoichiometry and by doping [18].

Zinc oxide is an important candidate used as sensing layer towards hazardous gases [19–21]. In general, ZnO gas sensors possess several advantages such as low cost, easy manufacturing, and small size, in comparison with the traditional analytical instruments. This oxide that can be prepared with different morphologies (nanoparticles, nanotubes, nanorods, etc.) has been largely studied for applications in gas sensors, because of its important optical, morphological, microstructural and electric properties. Nundy et al. fabricated flower shaped ZnO and suggested that it exhibited high response toward NOx gas at 25 °C compared to ammonia, acetone, CO, toluene [22]. Shaikh et al. noticed that ZnO nanorods obtained from a simple two step chemical method showed good selectivity toward 40 ppm of NO2 gas and excellent repeatability at lower gas concentration of 2 ppm [23]. Kanaparthi et al. demonstrated that ZnO nanoflakes were very sensitive toward 80% of NH3 at 250 °C [24]. Kim et al. reported that ZnO nanofibers (NFs) synthesized by the simple electrospinning technique exhibited strong response and high selectivity toward 10 ppm of H_2 gas [25].

✉ M. Hjiri
m.hjiri@yahoo.fr

1 Department of Physics, Faculty of Sciences, King Abdulaziz University, Jeddah 21589, Saudi Arabia

2 Laboratory of Physics of Materials and Nanomaterials Applied at Environment, Faculty of Sciences of Gabes, 6072 Gabes, Tunisia

3 Center of Nanotechnology, King Abdulaziz University, Jeddah, Saudi Arabia

4 Department of Engineering, University of Messina, 98166 Messina, Italy

ZnO nanoparticles were obtained by several techniques such as hydrothermal [21], ball milling [26], co-precipitation [27], sol–gel [28] etc… The sol–gel is the most used process because it is low cost, simple and easy to control.

Photoluminescence (PL) is a largely used technique for defects detection in ZnO band gap [29–33]. It is well recognized that PL spectra of ZnO exhibits mainly two peaks, near band emission (NBE) in the UV range, due to the excition recombination [34] and a visible emission bands originating from the extrinsic and extrinsic defects in ZnO such as Vo [35], Zni [36] and Oi [37] and Vzn [38].

Carbon monoxide (CO), called the silent killer, is a hazardous gas that causes death. The incomplete combustion of fuels produced CO gas. This colorless and odorless toxic gas is found in the emission of automobile exhausts, the burning of domestic fuels. Carbon monoxide affects strongly human health even at low concentration. At low levels (above 70 ppm), CO can cause fatigue and nausea. CO causes disorientation and death at concentrations above 150 to 200 ppm [39]. Then it is important to fabricate and use CO gas sensors.

In present work, ZnO nanoparticles were prepared by sol–gel technique for the detection of CO gas. XRD, SEM and TEM were performed to investigate the structural and morphological properties of the material. In order to have an idea about the defects in the structure of ZnO, PL measurements are carried. Sensing tests were performed to show the sensing properties.

2 Experiments

2.1 ZnO Preparation

The sol–gel route was used to elaborate ZnO nanoparticles using 16 g of zinc acetate ($Zn(CH_3CO_2)_2 \cdot 2H_2O$) in 112 ml of methyl alcohol. After magnetic stirring for 15 min, 200 ml of ethanol were added to the solution. The obtained solution was poured in an autoclave and dried in supercritical conditions of ethyl alcohol (Tc = 243 °C; Pc = 63.6 bars) [40]. The obtained powders were subsequently heat treated at 400 °C for 2 h in air.

2.2 Sensing Test

We fabricated ZnO based sensor by printing a film of thickness around 1–10 μm of the paste of ZnO powders on alumina substrate. The substrate had dimensions of 6 mm × 3 mm with platinum interdigitated electrodes and platinum heater on the backside. The sensor device and structure are reported in Fig. 1. The sensors were then introduced in the testing chamber. The temperature measurements were in the range of 50–400 °C under a synthetic dry air. We utilized mass flow controllers to dilute the gases coming from certified bottles in air at a given concentration. The sensor response, S, is defined as $S = R_a/R_g$ $S = R_0/R$ where R_a is the resistance before gas injection in dry synthetic air (20% O_2 in nitrogen) and R_g is the electrical resistance of the sensor after gas injection.

Fig. 1 Sensor device and structure
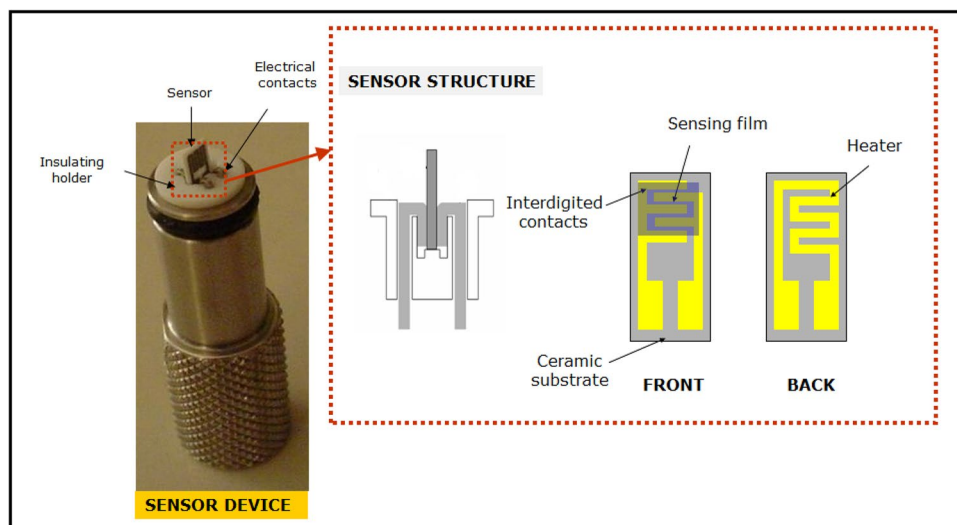
3 Results and Discussion

3.1 Microstructure and Morphology

Figure 2 presents the XRD spectrum of ZnO sample synthesized by sol–gel technique and treated at 400 °C for 2 h. The pattern shows various diffraction peaks assigned to ZnO with no secondary phases or impurities. The obtained ZnO powder is polycrystalline, its pattern is composed of different diffraction planes namely (100), (002), (101), (102), (110), (013), (112) and (021) which are characteristic of the Wurtzite hexagonal structure of ZnO according to JCPDS database (Card 36-1451) [41]. The lattice parameters and d-spacing, calculated from (002) peaks are a = 3.250 Å, c = 5.206 Å and d = 0.26 nm which are very close to ZnO structure [42].

The average crystallite size estimated by Scherer's equation has been estimated to be equal to 53 nm.

$$D = \frac{0.9\lambda}{B\cos\theta_B} \qquad (1)$$

where λ is the X-ray wavelength, θ_B is the maximum of the Bragg diffraction peak (in radians) and B is the full width at half maximum (FWHM) of the XRD peak.

Figure 3 reports SEM and TEM images presenting the morphology of ZnO nanopowders after annealing at 400 °C for 2 h. ZnO nanopowders were composed of agglomeration of uniform spherical grains. From TEM small ZnO nanoparticles with nanometric size are shown. The shape of crystallites is prismatic with a narrow distribution of particle size. The size of the majority of particles is around 50 nm which is in good agreement with the average crystallite size, D, deduced from XRD pattern.
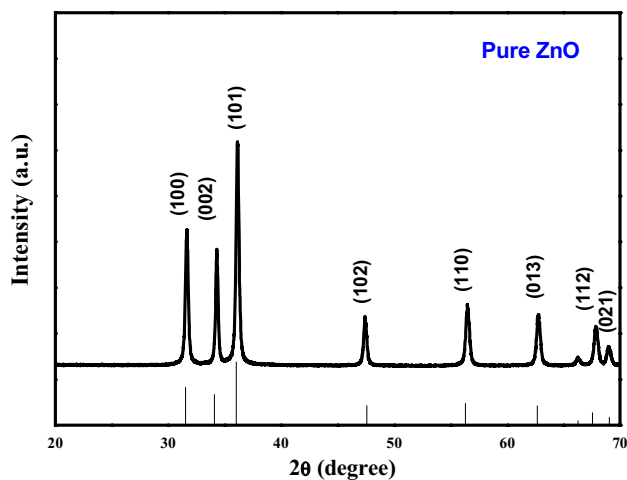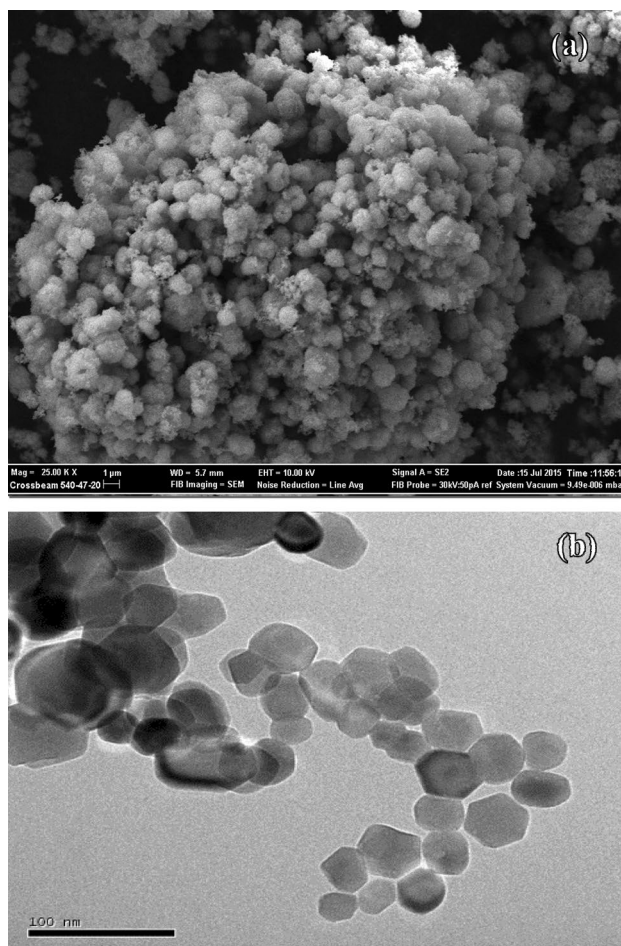

Fig. 3 a SEM and **b** TEM photographs of ZnO nanoparticles annealed at 400 °C

Fig. 2 XRD spectrum of ZnO nanoparticles calcinated at 400 °C for 2 h
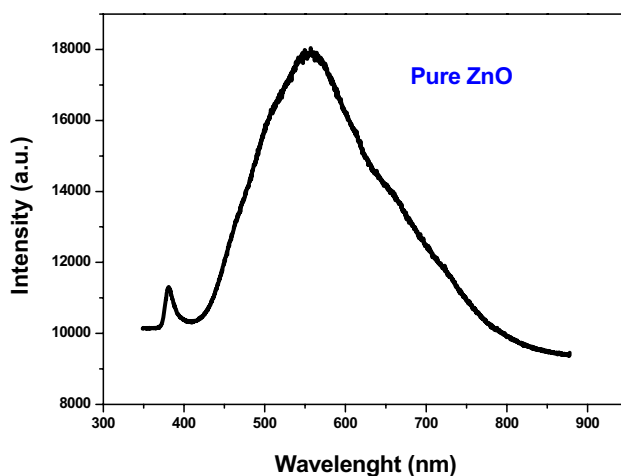

Fig. 4 Photoluminescence spectrum of ZnO nanoparticles

Figure 4 presents the photoluminescence spectrum recorded from pure ZnO sample in the wavelength range between 350 and 850 nm at room temperature. Two peaks are observed in the photoluminescence spectrum. The first peak is located at 380 nm and it corresponds to the near band edge (NBE) peak, it is due to the recombination of free excitons of ZnO [43]. The second peak is centered at around 554 nm. It is well known that the green emission originated from the electronic defects in the ZnO forbidden band, Therefore PL emission is a powerful method for electronic defect determination in semiconductors.

To determine the origin of the PL green emission centered at 544 nm, we have proceeded to a Gaussian deconvolution of this peak (Fig. 5). As shown, the green emission spectrum is composed of four peaks. The peak located at 466 nm (2.65 eV) originates from the transition from conduction band to oxygen vacancy defect V_o, the peak located at 500 nm (2.47 eV) is due to the transition from conduction band towards the interstitial oxygen defect (Oi), the peak at 546 nm (2.26 eV) is assigned to the transition from zinc interstitial defect (Zn_i) to oxygen vacancy defect level (V_o) and the peak at 651 nm (1.90 eV) is due to the transition from the complex VoZni to the defect Oi. Several authors have observed the same defect in ZnO band gap and PL peak position [35–38].

3.2 Sensing Properties

Figure 6 presents the variation of the resistance of ZnO nanopowders versus different operating temperatures. The higher resistance at low temperature can be explained by the disorder in the lattice which enhances the efficiency of scattering mechanism such as phonon scattering. As seen in Fig. 6, increasing the measurement temperature yields to the resistance decreases because of the thermal excitation
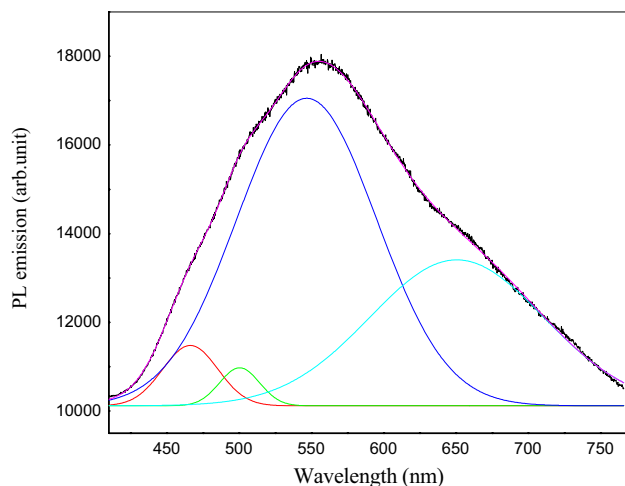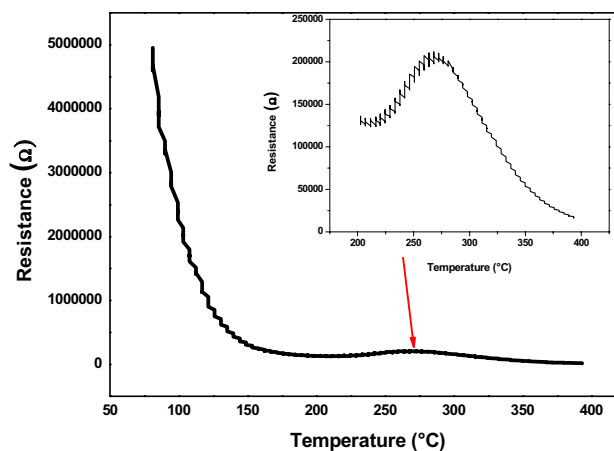

Fig. 6 Variation of Resistance as a function of temperature in air

of electrons into the conduction band indicating the semiconductor behavior of ZnO phase. It is well established that ZnO is an n-type semiconductor with a wide band gap of 3.2 eV [44]. The broad peak at around 270 °C shown in the insert figure is due to the oxygen chemisorption on surface material. The chemisorbed oxygen species reduces the electrons concentration, thereafter the resistance enhancement as shown in insert Fig. 6.

The measured activation energy of the electrical conductivity is estimated from Arrhenius plot as shown in Fig. 7; the obtained activation energy is about 0.48 eV. It is worth noting that the conductivity activation energy correspond to the Fermi level regarding the minimum conduction position, the low value of calculated activation energy (0.48 eV) indicates clearly that the prepared ZnO material is an n-type semiconductor. On the other hand, it is well known that the unintentional intrinsic defects in ZnO such as oxygen
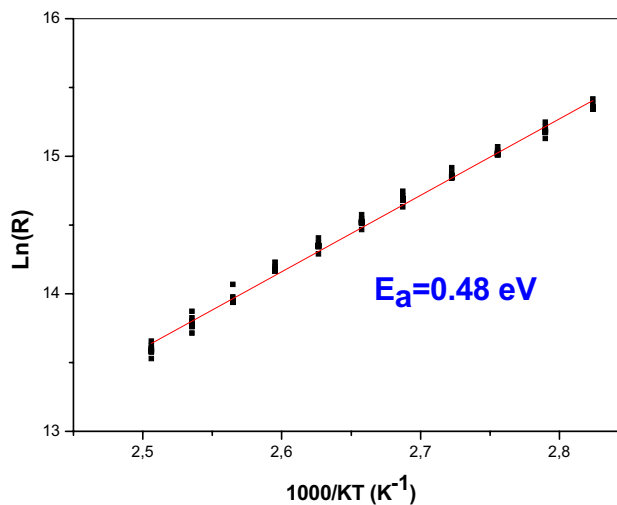

Fig. 5 Deconvolution of the PL green emission

Fig. 7 Activation energy calculated from Arrhenius plot

vacancy (Vo), interstitial oxygen (O_i) and interstitial Zn (Zn_i) act as donor defects, this explain the origin of n-type conduction in undoped ZnO. Thereafter, the low activation energy is consistent with the presence of donor defects (O_i, Zn_i and V_o) in the forbidden band as deduced from PL measurement (Fig. 5).

3.2.1 Response Towards CO Gas

The variation of ZnO sensor response versus temperature towards 80 ppm of carbon monoxide is shown in Fig. 8. The response exhibits a Gaussian shape. Starting from 150 °C, the response increases and goes through a maximum value located at 250 °C and then decreases. The CO sensor response depends on an accurate equilibrium between adsorption and desorption rate of carbon monoxide. It depends also on the reactivity of the CO surface with adsorbed oxygen. Enhancing temperature to some value leads to CO chemisorption and reaction rate occurring on the ZnO surface which favors increase of the gas response. Raising temperature, we showed a reduction on the gas response because of CO desorption; and this produces a decrease of the amount of carbon monoxide adsorbed on the surface of ZnO.

The dynamic responses of ZnO based sensor tested to different carbon monoxide concentrations from 5 to 80 ppm in air at different operating temperatures (200–350 °C) are reported in Fig. 9. The injection of CO gas decreases the electrical resistance of the layer. The signal could be back to its primary value after many cycles indicating that CO adsorption was reversible. The CO gas was then desorbed when the gas was turn off.

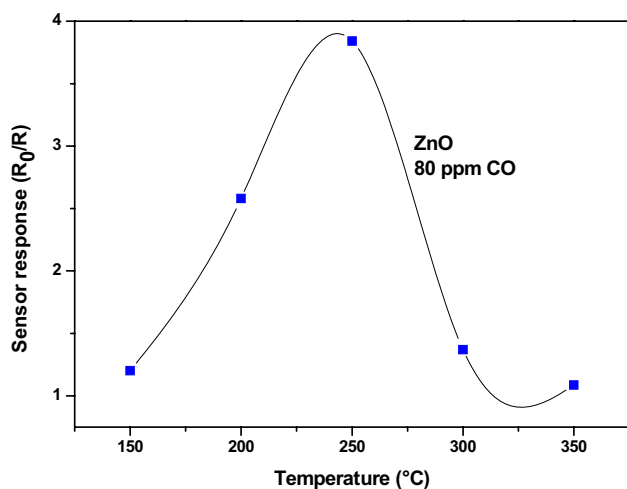The operating temperature is an important parameter that influences the sensor response; for 200 °C there was a remarkable drift when we have tested the sensor with different CO concentrations. The response was enhanced when the operating temperature increased to 250 °C and reached 3.8 and the drift disappeared. When the temperature increases to 300–350 °C, the sensor response gets decreases. The sensing mechanism can be explained as follow: Stable oxygen ions species were O_2^- below 200 °C, O^- between 200 and 300 °C, and O^{2-} above 300 °C [45]. The reactions of the oxygen species with CO molecules at different operating temperatures can be described using the following equations:

$$2CO + O_2^- \rightarrow 2CO_2 + e^- \tag{2}$$

$$CO + O^- \rightarrow CO_2 + e^- \tag{3}$$

$$CO + O^{2-} \rightarrow CO_2 + 2e^- \tag{4}$$

At temperature below 200 °C, Eq. 2 plays major role. In this case CO gas reacts slowly with O_2^- species leading to low response of the gas sensor. Going from 250 to 300 °C, the chemisorbed oxygen species present at the surface of ZnO are O^- and O^{2-}. This means that both Eqs. (3) and (4) participated in CO adsorption operation causing an increase of gas response. The previous mechanism can also explained in Fig. 10. Above 300 °C, only Eq. (3) appears in CO adsorption; and this explains the decrease of the response.

The response/recovery times is defined as the time which occurs to reach 90% of the final resistance after the exposure to target and reference air, respectively [46, 47].

The response and recovery time observed for ZnO sample with different operating temperature were 17–63 s and 30–102 s respectively as seen in Fig. 11. Faster response time is observed for the operating temperature of 300 °C and faster recovery time is observed at 350 °C. Lower response and recovery time, respectively 63 s and 102 s, were observed for the operating temperature of 200 °C. This is due to CO adsorption and desorption in the surface of the material.

3.2.2 Selectivity of ZnO Sensor

The fabricated device was tested to different gases such as CO, NO_2 and CO_2 at 250 °C in order to show the selectivity of the sensor. As seen in Fig. 12, the sensor device is very sensitive to CO gas. The response to oxidizing gases (such as NO_2) appears instead to be more limited. The selectivity of our sensor towards CO gas id attributed to many factors such as metal oxide shape and size. The operating temperature [48] is a key parameter for the selectivity of the gas sensor. CO molecules are very reactive from 250 to 350 °C. As result the sensor is selective to CO gas compared to CO_2 and NO_2.
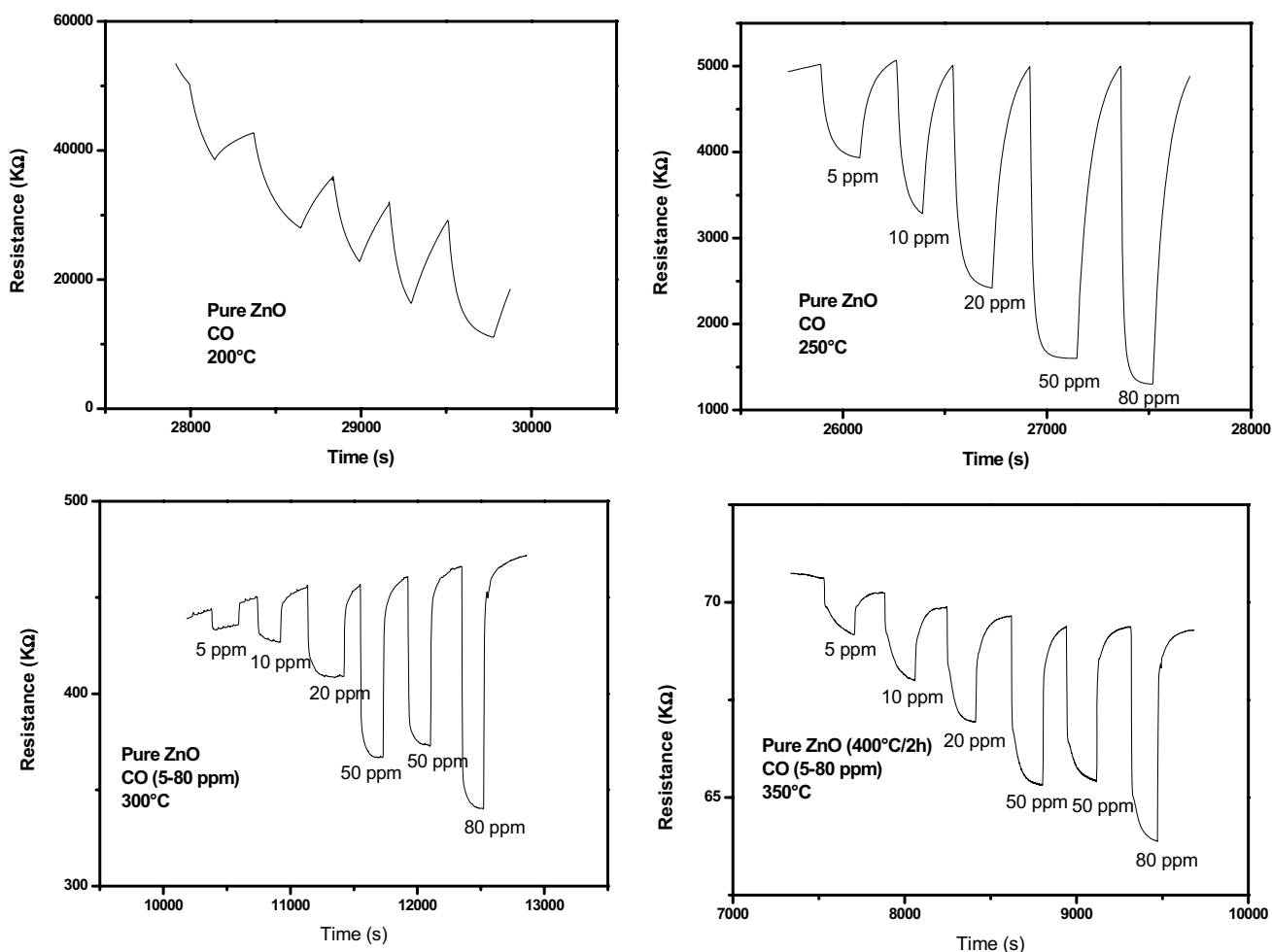

Fig. 8 Response to 80 ppm CO of the ZnO nanoparticles as a function of the temperature

Fig. 9 Dynamic response of pure ZnO at different operating temperature to various concentrations of CO in air
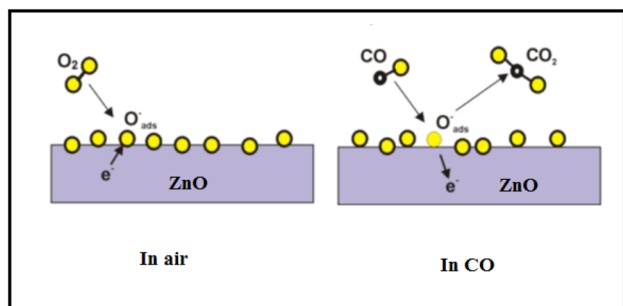

Fig. 10 CO sensing mechanism of ZnO gas sensor

In order to show the stability of the sample, ZnO was tested towards 80 ppm of CO at 250 °C several times along 1 months as seen in Fig. 13. We noticed that the sensor response decreases from 74 to 71%. This is probably due to the surface reaction with its surroundings along the measurements. The sample exhibited a high durability of around 95%.
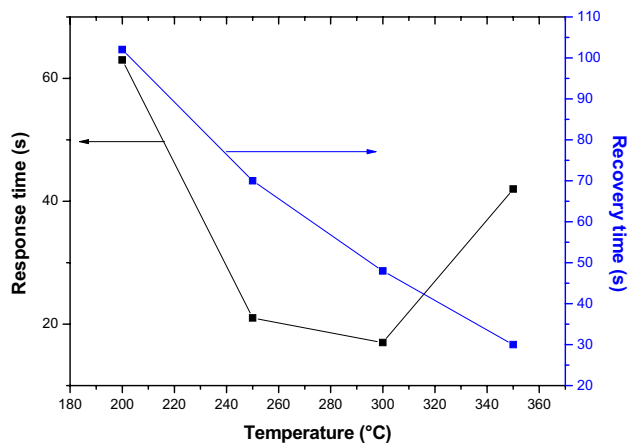

Fig. 11 Variation of response/recovery times versus operating temperature
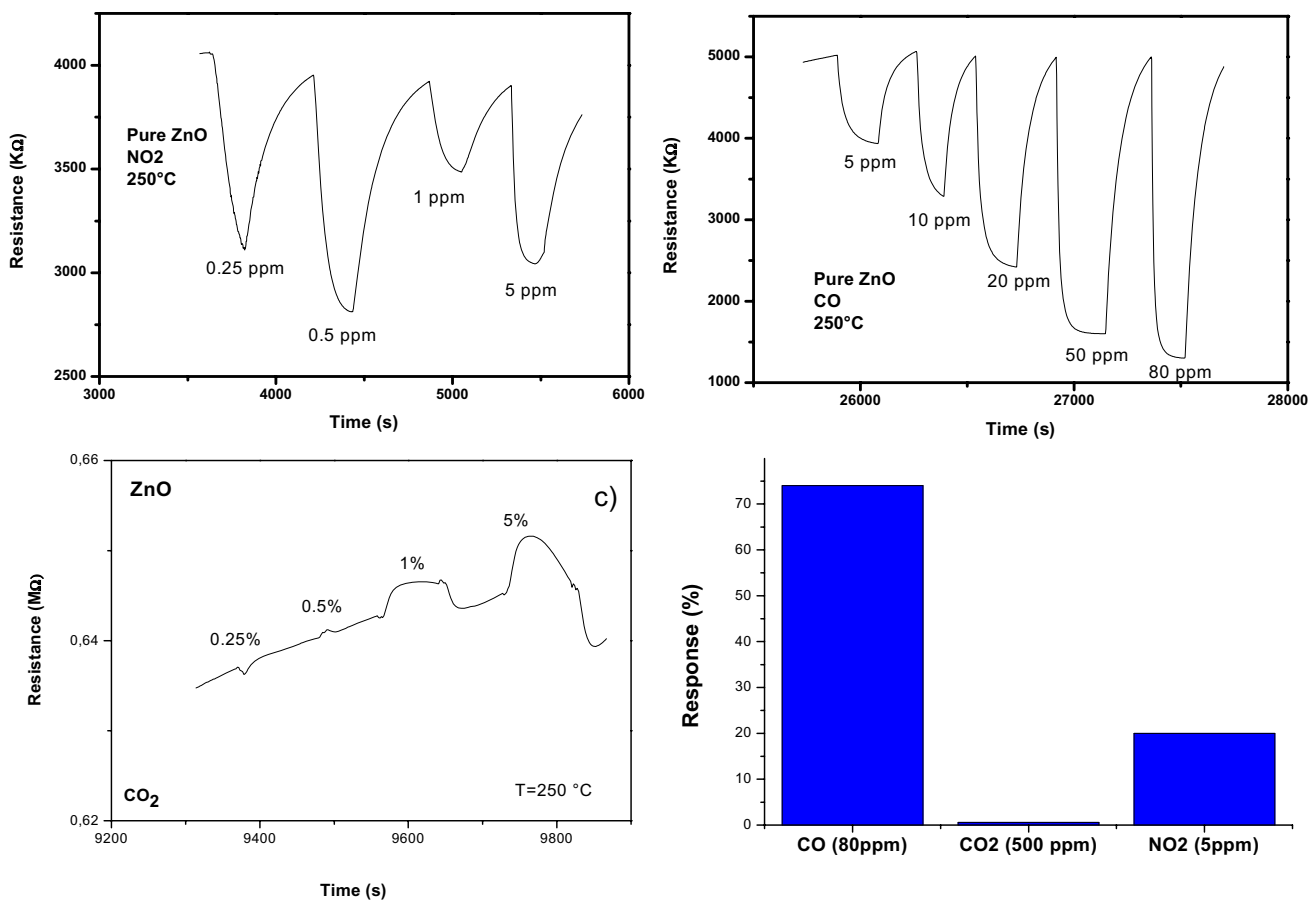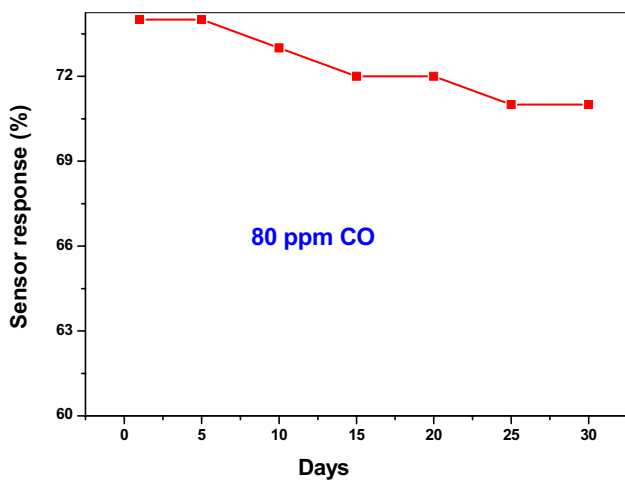
Fig. 12 Response to different gases

Fig. 13 Stability of the sensor with days towards 80 ppm of CO gas

Fig. 14 Reproducibility tests to 80 ppm of CO at 250 °C
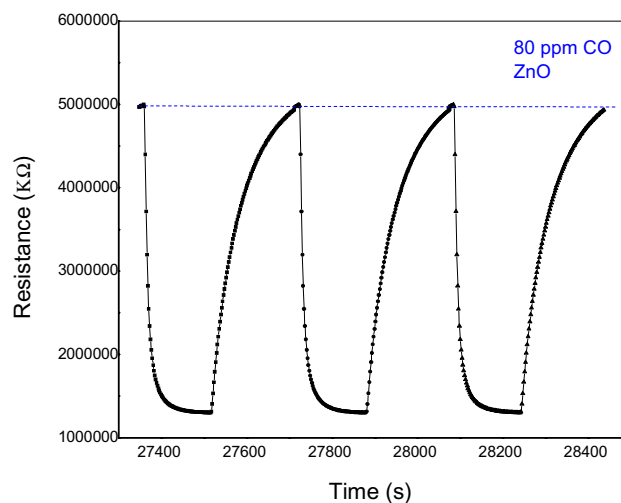
Figure 14 presents the reproducibility of the sensor when exposed to three consecutive pulses of 80 ppm of CO gas at 250 °C. It is clearly observed that the response and recovery characteristics are almost reproducible.

As shown in Table 1, the developed sensor based on ZnO nanopowders shows a very high response and quick response/recovery times compared to a previous works

Table 1 Comparison of different CO sensing properties with other works

Sample	Response (%)	CO (ppm)	Temperature (°C)	Response time (s)	Recovery time (s)	Refs.
ZnO	74	80	250	21	70	This work
Sm_2O_3	34	50	250	35	110	[49]
TiO2/LSCN	38.4	400	200	–	–	[50]
$LaCo_{1-x}Fe_xO_3$	40.9	100	250	187	100	[51]
CuO	47.2	800	150	40	90	[52]

[49–52]. A response, $(\Delta R/R0)$ % of 74 at 80 ppm, is obtained which indicates the high sensor response of our device as CO gas sensor.

4 Conclusion

Pure ZnO nanoparticles have been prepared by sol–gel technique and heat treated at 400 °C for 2 h in air. ZnO nanoparticles have a hexagonal wurtzite structure with an average crystallite size of 50 nm. TEM showed spherical and agglomerated particles with a size of about 50 nm. PL measurements showed two peaks are observed in the photoluminescence spectrum. The first peak is located at 380 nm and it corresponds to the near band edge (NBE) peak and the second peak is centered at around 554 nm. It is well known that the green emission originated from the electronic defects in the ZnO forbidden band. The realized gas sensor exhibited a high response of 74% towards 80 ppm of CO gas at 250 °C. The response/recovery times are 21 and 70 s, respectively. The fabricated sensor has been tested to CO_2 and NO_2 gases. The results reveal its high response towards CO in comparison to the other studied gases. In addition our sensor exhibited good reproducibility and long stability. The good sensing properties of ZnO nanoparticles towards CO gas suggests its potential application for the detection of this hazardous gas.

References

1. Z.D. Lin, W.L. Song, H.M. Yang, Sens. Actuators B **173**, 22–27 (2012)
2. P. Sun, W.N. Wang, Y.P. Liu, Y.F. Sun, J. Ma, G.Y. Lu, Sens. Actuators B **173**, 52–57 (2012)
3. H. Kim, C. Jin, S. Park, S. Kim, C. Lee, Sens. Actuators B **161**, 594–599 (2012)
4. P.M. Perillo, D.F. Rodríguez, Sens. Actuators B **171–172**, 639–643 (2012)
5. C. Baban, Y. Toyoda, M. Ogita, J. Optoelectron. Adv. Mater. **7**, 891–896 (2005)
6. J.J. Hassana, M.A. Mahdia, C.W. China, H. Abu-Hassan, Z. Hassan, Sens. Actuators B **176**, 360–367 (2013)
7. P. Singh, V.N. Singh, K. Jain, T.D. Senguttuvan, Sens. Actuators B **166–167**, 678–684 (2012)
8. K. Omri, A. Bettaibi, K. Khirouni, L. El Mir, Phys. B **537**, 167–175 (2018)
9. K. Omri, A. Alyamani, L. El Mir, J. Mater. Sci. **30**, 16606–16612 (2019)
10. K. Omri, I. Najeh, L. El Mir, Ceram. Int. **42**, 8940–8948 (2016)
11. R.N. Viswanath, S. Ramasamy, R. Ramamoorthy, P. Jayavel, T. Nagarajan, Nanostruct. Mater. **6**, 993–996 (1995)
12. M.S. Wu, A. Azuma, T. Shiosaki, A. Kawabata, I.E.E.E. Trans, Ultrason. Ferroelec. Freq. Contr. **136**, 442–445 (1989)
13. M.K. Jayaraj, A. Antony, M. Ramachandran, Bull. Mater. Sci. **25**, 227–230 (2002)
14. K. Keis, C. Bauer, G. Boschloo, A. Hagfeldt, K. Westermark, H. Rensmo, H. Siegbahn, J. Photochem. Photobiol. A **148**, 57–64 (2002)
15. P. Yang, H. Yan, S. Mao, R. Russo, J. Johnson, R. Saykally, N. Morris, J. Pham, R. He, H. Choi, Adv. Funct. Mater. **12**, 323–331 (2002)
16. S. Roy, S. Basu, Bull. Mater. Sci. **25**, 513–515 (2002)
17. A.R. Raju, C.N.R. Rao, Sens. Actuators B **3**, 305–310 (1991)
18. L. El Mir, Z. Ben Ayadi, M. Saadoun, H.J. Von Bardeleben, K. Djessas, A. Zeinert, Phys. Status Solidi (a) **204**, 3266–3277 (2007)
19. T. Yamazaki, S. Wada, T. Noma, T. Suzuki, Sens. Actuators B **13–14**, 594–595 (1993)
20. M. Hjiri, L. El Mir, S.G. Leonardi, A. Pistone, L. Mavilia, G. Neri, Sens. Actuators B **196**, 413–420 (2014)
21. E. Pál, V. Hornok, R. Kun, A. Oszkó, T. Seemann, I. Dékány, M. Busse, J. Colloid Interface Sci. **378**, 100–109 (2012)
22. S. Nundy, T. Eom, J. Kang, J. Suh, M. Cho, J.S. Park, H.J. Lee, Ceram. Int. **46**, 5706–5714 (2020)
23. S.K. Shaikh, V.V. Ganbavale, S.V. Mohite, U.M. Patil, K.Y. Rajpure, Superlattices Microstruct. **120**, 170–186 (2018)
24. S. Kanaparthi, S.G. Singh, Mater. Sci. Energy Technol. **3**, 91–96 (2020)
25. J.H. Kim, A. Mirzaei, H.W. Kim, P. Wu, S.S. Kim, Sens. Actuators B **293**, 210–223 (2019)
26. J. Singh, S. Sharma, S. Soni, S. Sharma, R. Chand Singh, Mater. Sci. Semicond. Process. **98**, 29–38 (2019)
27. P. Shunmuga Sundaram, S. Stephen Rajkumar Inbanathan, G. Arivazhagan, Phys. B **574**, 411668 (2019)
28. M. Hjiri, R. Dhahri, L. El Mir, A. Bonavita, N. Donato, S.G. Leonardi, G. Neri, J. Alloys, Compounds **634**, 187–192 (2015)
29. J.L. Yu, Y.F. Lai, S.Y. Cheng, Q. Zheng, Y.H. Chen, J. Lumin. **161**, 330–334 (2015)
30. J. Lv, M. Fang, Mater. Lett. **218**, 18–21 (2018)
31. S. Pal, A. Sarkar, P. Kumar, D. Kanjilal, T. Rakshit, S.K. Ray, D. Jana, J. Lumin. **169**, 326–333 (2016)
32. J.D. McNamara, N.M. Albarakati, M.A. Reshchikov, J. Lumin. **178**, 301–306 (2016)
33. J. Wang, S. Yu, H. Zhang, Optik **180**, 20–26 (2019)
34. C. Wende, W. Ping, Z. Xingquan, X. Tan, J. Appl. Phys. **100**, 5 (2006)

35. T.M. Børsetha, B.G. Svensson, A.Y. Kuznetsov, Appl. Phys. Lett. **89**, 26 (2006)
36. K. Ravichandran, A. Anbazhagan, M. Baneto, N. Dineshbabu, C. Ravidhas, G. Muruganandam, Mater. Sci. Semicond. Process. **41**, 150–154 (2016)
37. P. Murkute, H. Ghadi, S. Saha, S.K. Pandey, S. Chakrabarti, Mater. Sci. Semicond. Process. **66**, 1–8 (2017)
38. P.U. Londhe, N.B. Chaure, Mater. Sci. Semicond. Process. **60**, 5–15 (2017)
39. G. Neri, A. Bonavita, G. Micali, G. Rizzo, E. Callone, G. Carturan, Sens. Actuators B **132**, 224–233 (2008)
40. L. El Mir, J. El Ghoul, S. Alaya, M. Ben Salem, C. Barthou, H.J. von Bardeleben, Phys. B **403**, 1770–1774 (2008)
41. Y. Chen, D.M. Bagnall, H.K. Koh, K.T. Park, K. Hiraga, Z.Q. Zhu, T. Yao, J. Appl. Phys. **84**, 3912 (1998)
42. Y. Chem, D.M. Bagnall, H.K. Koh, K.T. Park, K. Hiraga, Z.Q. Zhu, T. Yao, J. Appl. Phys. **84**, 3912 (1998)
43. V.A. Fonoberov, K.A. Alim, A.A. Balandin, F. Xiu, J. Liu, Phys. Rev. B **73**, 165317–165326 (2006)
44. D.R. Lide, *Handbook of Chemistry and Physics* (CRC Press, Florida, 1992), pp. 4–163
45. H. Gong, J.Q. Hu, J.H. Wang, C.H. Ong, F.R. Zhu, Sens. Actuators B **115**, 247–251 (2006)
46. B.T. Raut, P.R. Godse, S.G. Pawar, M.A. Chougule, B. Patil, J. Mater. Sci. **23**, 956–963 (2012)
47. L.E. Mathevulaa, L.L. Notoa, B.M. Mothudia, M. Chithambo, M.S. Dhlamini, J. Lumines. **192**, 879–887 (2017)
48. M. Hjiri, L. El Mir, S.G. Leonardi, N. Donato, G. Neri, Nanomaterials **3**, 357–369 (2013)
49. S. Rasouli Jamnani, H. Milani Moghaddam, S.G. Leonardi, N. Donato, G. Neri, Appl. Surf. Sci. **487**, 793–900 (2019)
50. K.-C. Hsu, T.-H. Fang, Y.-J. Hsiao, P.-C. Wu, J. Alloy. Compd. **794**, 576–584 (2019)
51. J.-C. Ding, H.-Y. Li, T.-C. Cao, Z.-X. Cai, X.-X. Wang, X. Guo, Solid State Ionics **303**, 97–102 (2017)
52. R. Molavi, M.H. Sheikhi, Mater. Sci. Semicond. Proc. **106**, 104767 (2020)

Publisher's Note Springer Nature remains neutral with regard to jurisdictional claims in published maps and institutional affiliations.